MATERIALS SCIENCE

Electron videography of a lipid–protein tango

John W. Smith[1], Lauren N. Carnevale[2], Aditi Das[3]*, Qian Chen[1,4,5,6]*

Biological phenomena, from enzymatic catalysis to synaptic transmission, originate in the structural transformations of biomolecules and biomolecular assemblies in liquid water. However, directly imaging these nanoscopic dynamics without probes or labels has been a fundamental methodological challenge. Here, we developed an approach for "electron videography"—combining liquid phase electron microscopy with molecular modeling—with which we filmed the nanoscale structural fluctuations of individual, suspended, and unlabeled membrane protein nanodiscs in liquid. Systematic comparisons with biochemical data and simulation indicate the graphene encapsulation involved can afford sufficiently reduced effects of the illuminating electron beam for these observations to yield quantitative fingerprints of nanoscale lipid–protein interactions. Our results suggest that lipid–protein interactions delineate dynamically modified membrane domains across unexpectedly long ranges. Moreover, they contribute to the molecular mechanics of the nanodisc as a whole in a manner specific to the protein within. Overall, this work illustrates an experimental approach to film, quantify, and understand biomolecular dynamics at the nanometer scale.

INTRODUCTION

In a *Noh* drama, a flamenco dance, or one of the great silent films, form, gestures, and motion tell the story, revealing the traits and relationships of the characters. Although occurring on a smaller stage, the motions of biomolecules do the same. As they transform from one configuration to another, in native or perturbed states, proteins, lipids, and nucleic acids recount the "tales" of enzymatic catalysis, synaptic transmission, DNA replication, etc. Biological processes are built upon these dances (*1*), with structural and dynamical elements both defined by liquid water (*2*). Not only does water define the hydrophobic collapse and smooth energy barriers en route to protein folding, but it also facilitates communication between molecules or subunits and may enhance or suppress flexibility, in which cases its own dynamical properties enter into biomolecular function (*2*, *3*). In short, fully understanding biomolecular processes and interactions in context calls for interrogation of both structure and structural dynamics, at the individual level, and in liquid, but meeting all these criteria is technically challenging. While spectroscopy- or scattering-based approaches can reveal structural and dynamical traits simultaneously and with high spatiotemporal resolution (*4*–*6*), their level of insight is limited to information that can survive ensemble averaging. Work in microscopy, on the other hand, strives to film individuals (*7*–*10*), but optical methods (*10*, *11*), even super-resolution methods with labels, still find it challenging to reveal submolecular structural details. Approaches based on electron microscopy, meanwhile, have the requisite nanometer (or better) spatial resolution (*12*, *13*), but in electron microscopy, the crux of challenges has been an incompatibility with liquid, limiting its scope to the study of fixed or frozen (i.e., immobilized) specimens. Single-particle analysis methods used in cryo-electron microscopy can sometimes be used to infer dynamical information indirectly, but flexible motifs are generally lost to averaging. These approaches also demand high uniformity—and therefore laborious purification of just a few structural states—which may come at the cost of meaningful molecular individuality.

Here, we present electron videography of suspended biomolecular assemblies in liquid, harnessing liquid phase transmission electron microscopy (TEM), molecular modeling, and biophysical theory (Fig. 1, A to E, and fig. S1). Liquid phase TEM implements vacuum-tight, electron transparent chambers to preserve fully solvated specimens in the vacuum of an electron microscope. The technique itself has been growing steadily in the materials science community (*14*–*17*), but efforts to film biomolecules have been confounded by their low stability and visibility. Previous work has achieved snapshots of viruses (*18*), structural proteins (*19*, *20*), and cells (*21*) and in the process identified some protocols for sample preparation and imaging that help mitigate electron beam damage (*20*, *22*), but continuous protein dynamics have not yet been observed. With careful adaptations of encapsulation methods, electron dose rates, and total doses (texts S1 to S3), here we achieved real-time imaging for highly extended periods, with morphology sampling sufficient to pair our observations with molecular dynamics (MD) simulations (*23*) and biophysical models (*24*), and capture rare events. Unexpectedly, our systematic comparisons with available biochemical and biophysical data described below suggest that the specimen sustains a sufficiently reduced amount of damage from imaging electrons—likely due to graphene encapsulation (see text S1 and later discussion)—to yield meaningful insight. Through synergy of several possible mechanisms (text S1), graphene encapsulation appears to reduce or at least postpone radiolysis to an extent that makes it possible to capture dynamics that are shown to be consistent with both theory and simulation. Although the spatial resolution is not yet at the level of cryo-TEM (where many thousands of individual images are combined) and functional groups may not be completely preserved, the obtained molecular movies reveal the liquid phase structure of these assemblies individually and in submolecular detail without averaging (Fig. 1, F to K) and make it possible to quantify roles of intermolecular interactions in their dynamics.

[1]Department of Materials Science and Engineering, University of Illinois Urbana–Champaign, Urbana, IL 61801, USA. [2]Department of Biochemistry, University of Illinois Urbana–Champaign, Urbana, IL 61801, USA. [3]School of Chemistry and Biochemistry, Parker H. Petit Institute for Bioengineering and Biosciences, Georgia Institute of Technology, Atlanta, GA 30332, USA. [4]Beckman Institute for Advanced Science and Technology, University of Illinois Urbana–Champaign, Urbana, IL 61801, USA. [5]Department of Chemistry, University of Illinois Urbana–Champaign, Urbana, IL 61801, USA. [6]Materials Research Laboratory, University of Illinois Urbana–Champaign, Urbana, IL 61801, USA.
*Corresponding author. Email: aditi.das@chemistry.gatech.edu (A.D.); qchen20@illinois.edu (Q.C.)

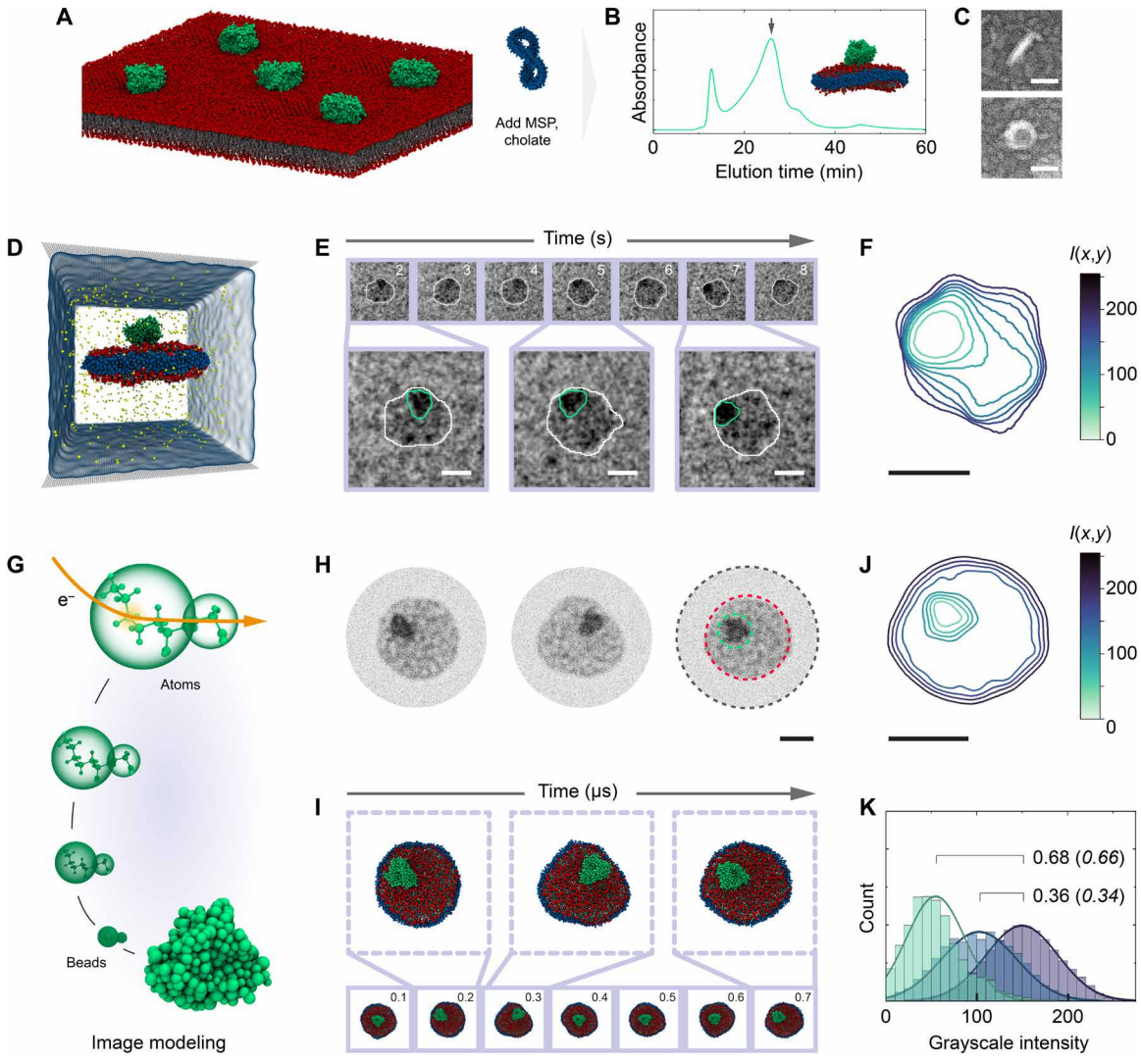

Fig. 1. Single-nanodisc imaging with liquid-phase TEM. (**A** and **B**) CYP2J2 (represented in green) was combined with lipids (represented with head groups in red and tail groups in gray) and MSPs (represented in blue) to form nanodiscs, with subsequent purification by size exclusion chromatography [fractions at the arrow (B) were collected for analysis]. (**C**) Negative stain micrographs—where nanodiscs appear bright against the high-atomic number stain background—showing representative elliptical and circular projections. (**D**) Suspended nanodiscs were then encapsulated in graphene chambers to image continuous morphology fluctuations using liquid phase TEM (**E**). (**F**) Contrast variations, highlighted with a representative intensity profile, *I*(*x*, *y*), reveal the shape, position, and orientation of CYP2J2[(E), green lines] in the plane of the membrane, within the overall nanodisc contour [(E), white lines]. (**G** to **J**) Experimental snapshots were compared with images simulated based on MD-generated coordinates (examples shown in I). Contrast variations in simulated images (J) matched well with experimental results (F). (**K**) The ratios of intensity between the background, lipid-only, and CYP2J2-containing areas [gray, red, and green, respectively, in (H), and right to left in (K)] show agreement between simulation and experiment (values in regular case are from experimental data, and values in italics are from simulation). Scale bars, 20 nm (C) and 10 nm [(E), (F), (H), and (J)].

In this work, we show how this unique imaging tool can provide insight into biological membrane systems and nanoscale lipid–protein interactions. In particular, we study membrane protein nanodiscs, membrane proteins in a dispersed, "single particle" form now commonly used for investigations of membrane protein structure (*25*), and an ideal model system for studying lipid–protein interactions (*26*). As membrane proteins participate in a wide variety of biological processes—signal transduction, ion transport, membrane metabolism, etc.—their interactions with lipids fine-tune their functionality, with lipids dictating the phase behavior, curvature, and other physicochemical properties of the membrane environment across a range of length and time scales (*27*, *28*). For example, previous work on nanodiscs using spectroscopy (*29*, *30*) and cryo-TEM (*26*) has shown how proteins are sensitive to local membrane fluidity, or how a few specific, tightly bound lipids can stabilize a protein's functional state(s). However, investigating longer length and time scales of lipid–protein interactions (*31*)—which might be found in whole-nanodisc behavior—has remained a challenge. Indeed, nanodiscs constitute an advantageous test bed for electron videography, as these important thermal fluctuations match the current resolution of the technique. Some understanding has come from MD simulations (*26*, *32*), but these efforts are generally limited to microsecond-scale

phenomena. Here, we image nanodisc structural fluctuations for minutes. We achieve high spatiotemporal resolution (nanometer, subsecond) while preserving complexities that are challenging to model computationally, lending quantitative insight into the fundamental molecular motions, mechanics, and lipid–protein interactions that govern nanodisc—and therefore membrane/membrane protein—structural dynamics at the nanometer scale.

RESULTS

We first investigated nanodiscs containing cytochrome P450 2J2 (CYP2J2) and stabilized with a long scaffold protein [membrane scaffold protein (MSP) 2N2; Fig. 1, A to C, and figs. S2 and S3] (*33*, *34*). CYP2J2 is a cardiac cytochrome P450 involved in arachidonic acid metabolism and a representative peripheral membrane protein whose assembly into nanodiscs is well established (*34*), whereas the long MSP imparts nanodiscs with a relatively large diameter that facilitates visibility. In graphene-based liquid chambers (Fig. 1D and figs. S1 and S4 to S8), the nanodiscs fluctuate and diffuse (fig. S9) for up to a few minutes before exhibiting obvious damage from the electron beam (fig. S6), so we monitored their projections over time (Fig. 1E, movie S1, and tables S1 and S2).

Moderate interactions with the substrate (text S2) serve to slow nanodiscs' translational, rotational, and internal motion enough to make both their position and structural features visible in individual exposures without (as is discussed in more detail below) overtly disrupting their fluctuations. More specifically, in free Brownian motion, nanodiscs would have Stokes–Einstein diffusion coefficients on the order of ~10^7 nm^2 s^{-1} in water, whereas diffusion coefficients calculated from experimental data were, on average, 1.2 nm^2 s^{-1}. Similarly, an autocorrelation analysis of the nanodisc radius of gyration from our MD simulations (Materials and Methods) suggests a structural relaxation time of 89.5 ± 3.5 ns, which is again much faster than experimentally observable time scales, yet the resolved structures still exhibit time-varying features down to the nanometer level (Fig. 1E). Previous works, using both liquid phase TEM (*35*, *36*) and high-speed atomic force microscopy (*9*, *37*), have also noted slowed molecular motion near interfaces. The behavior in our own experiments may be comparable to dynamics in supported lipid bilayers, in which lipid diffusion is known to be "biologically meaningful" but substantially slower than in unsupported membranes such as giant unilamellar vesicles (*38*–*41*). Thus, the shape fluctuations of the nanodisc as a whole are similarly slowed, which facilitates observation.

In cases with minor out-of-plane motion (text S4 and fig. S10), the shape, position, and orientation of CYP2J2 itself—as it diffuses and rotates within the nanodisc—can be directly discerned from intensity variations. (CYP2J2 is free to explore the interior of the nanodisc and veer "off center" in both experiment and simulation (figs. S10 to 16) because the membrane is fluid at room temperature and large compared to the protein. Similar behavior has been proposed based on results from small-angle scattering and cryo-TEM (*42*, *43*). In particular, we provide support that the roughly triangular features discernible in many frames (Fig. 1, E and F) have the form and contrast expected of CYP2J2 by comparing experimental TEM images to "synthetic" images simulated based on MD-generated coordinates (Fig. 1, G to I; table S3; and movie S2). Simulated images show qualitatively and quantitatively similar contrast variation to experimental video frames, with distinct intensities corresponding to the background, the membrane-only portion of the nanodisc, and the darkest region with the membrane protein (Fig. 1, F, J, and K).

This ability to localize and orient proteins in individual lipid–protein assemblies constitutes a major improvement over current experimental tools. Previous work required nanoparticle labels to monitor protein motion at high resolution (*21*, *44*)—an approach that cannot be used to reveal substructural detail and potentially induces abiological fluctuations—or only revealed topographical information (*37*). Our approach may therefore offer exciting opportunities to study positional and orientational dynamics during protein–protein interactions in a membrane environment, such as in docking or oligomer formation.

By revealing not only the shape of a nanodisc but also the extent of its fluctuations, electron videography can identify variations in nanodisc structure without averaging, even in the cases where out-of-plane rotation is present (Fig. 2, A to C). For example, if projections are fit to an ellipse (Fig. 2, A and B, and figs. S10 and S17), rotation and shape fluctuation manifest in variations of the minor and major axis, respectively (text S4). Nanodiscs with the long MSP display major axes in the range of 18 to 22 nm over time, in agreement with the MSP length (*45*) and negative stain TEM characterization (Fig. 1C and fig. S2). Nanodiscs prepared with a shorter MSP, however, MSP 1E3D1, are readily distinguishable, with major axes of 13 to 15 nm (Fig. 2D, fig. S2, and table S1). Meanwhile, empty nanodiscs—prepared with long MSPs but no CYP2J2—displayed major axes similar to filled ones (~20 nm) but of a broader statistical distribution (Fig. 2E and table S1). We attribute this broadening to the greater tendency of a nanodisc to fluctuate when hydrophobic or electrostatic interactions between the membrane and a protein are not present (Fig. 2C). Notably, this also suggests that lipid–membrane protein interactions influence fluctuations all the way up to the nanodisc boundary—a range of at least several nanometers—which is consistent with our MD simulations (figs. S11 to S15 and tables S1 and S2). Overall, these initial, comparative experiments highlight the ability to differentiate nanodiscs structurally, dynamically, and in a robust and quantitative way, with minimized apparent artifacts from the electron beam or substrate (texts S1 to S3). We therefore delved deeper to understand nanodisc properties observed in experiments.

The evolution of the nanodisc shape over time can also offer deeper and more quantitative biophysical insight (Fig. 3 and movie S1). When rotation is negligible, these undulatory motions involve (i) thermal fluctuations of the α-helical MSPs against constraints imposed by hydrogen bonding, (ii) the fluid-like motion of interior lipids (Fig. 3, C to E), and (iii) as suggested by the results above (Fig. 2E), a "dampening" effect from lipid–protein interactions. Phenomenologically, undulations decompose into contributions from a range of angular frequencies (Fig. 3C and fig. S18). A more physical interpretation of these contributions can be made by analyzing the Fourier square amplitude $\langle |u(q)|^2 \rangle$ across a range of wavevectors q (Fig. 3F and fig. S19) (*24*). In doing so, we find that nanodisc contour undulations can be described by two effective mechanical properties: a bending rigidity, κ, and a tension, σ, with experimental data following $\langle |u(q)|^2 \rangle = \frac{k_B T}{\kappa q^4 + \sigma q^2}$ ($k_B T$ denotes the thermal energy), such that $\langle |u(q)|^2 \rangle \sim q^{-2}$ in the low q regime (with corresponding fitted $\sigma = 4.6 \times 10^{-4}$ $k_B T$ nm^{-1}) and $\langle |u(q)|^2 \rangle \sim q^{-4}$ in the high q regime (with corresponding fitted $\kappa = 2.1$ $k_B T$ nm). The same regimes appear in equilibrium MD simulations, particularly in the high-q regime (Fig. 3F and fig. S19).

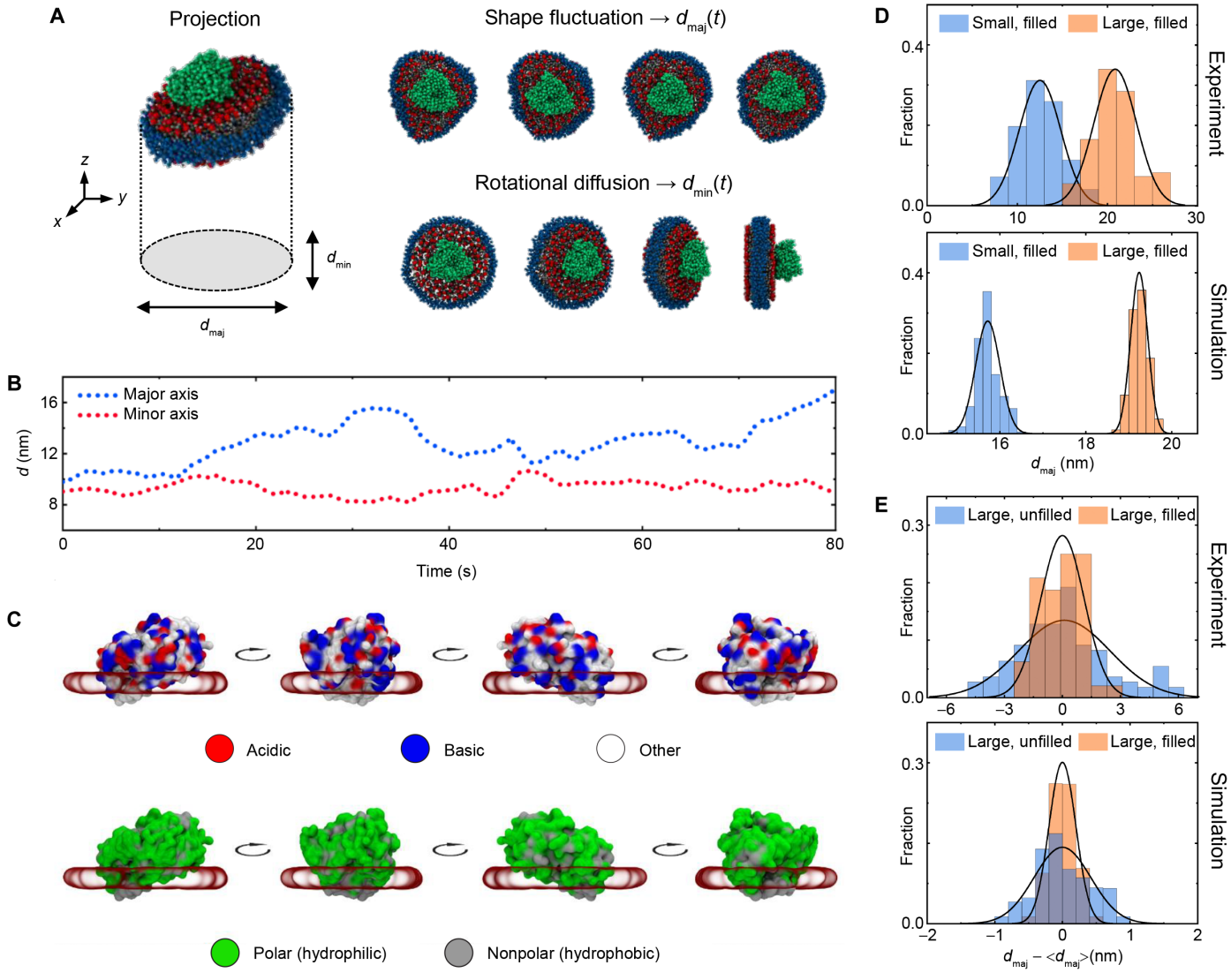

Fig. 2. Experimentally resolved fluctuations from a range of nanodiscs are consistent with MD simulations. (**A**) Rotationally diffusing nanodiscs present approximately elliptical projections which may be fit with a major and minor axis (d_{maj}, d_{min}). The major axis is sensitive predominantly to the overall shape fluctuations of the nanodisc, while the minor axis is mainly dependent on rotational diffusion (text S4). (**B**) The fact that both change over time suggests that nanodiscs exhibit both behaviors. (**C**) The behavior of d_{maj} over time is also affected by noncovalent (electrostatic and hydrophobic) interactions between CYP2J2 and the membrane; when present, they dampen the overall nanodisc fluctuations and therefore reduce the variability of d_{maj}. Views in (C) depict the specific distribution of charged and hydrophobic residues across CYP2J2 that may interact with the membrane. (**D**) Nanodiscs prepared with different MSPs are readily distinguished based on the magnitude of d_{maj}. "Small" here refers to nanodiscs prepared with MSP 1E3D1, while "large" refers to nanodiscs prepared with MSP 2N2. The relatively wider distributions observed in experiments (D), top] may be attributed to minor motion blur. (**E**) Nanodiscs prepared with and without a membrane protein ("filled" versus "unfilled," respectively), on the other hand, can be distinguished based on the variance of d_{maj}. The higher variance in the protein-free case may be attributed to the lack of dampening lipid–protein interactions.

We note that these parameters are apparently not perturbed by the graphene substrate, with experimental data closely matching "control" simulations where graphene (and beam effects) are not considered (text S3 and figs. S20 and S21). In addition, a comparable bending rigidity has been measured for high density lipoprotein particles—structurally similar assemblies—using nanoindentation (*46*), although a tension has not been previously described. We anticipate that these measures are sensitive to protein content and to the lipids' phase behavior, fluidity, or curvature and offer a metric for future comparative studies. Our simulations show that subtle differences can be detected even for two very closely related peripheral membrane proteins, CYP2J2 and its relative CYP3A4 (Fig. 3F). In other words, nanodisc undulations are a fingerprint of specific lipid–protein interactions, which may be related to domain behavior in full biological membranes. In this system, the interfacial mechanics generally "penalize" deformation, restricting nanodiscs to a round shape. Contours are well described by a single circular domain, and local frame-to-frame "flow" (Fig. 3, D and E) is small and symmetric, with the area changing <4%. These mesoscale flows can be directly related to the diffusion of single lipid molecules in simulations (Fig. 3E).

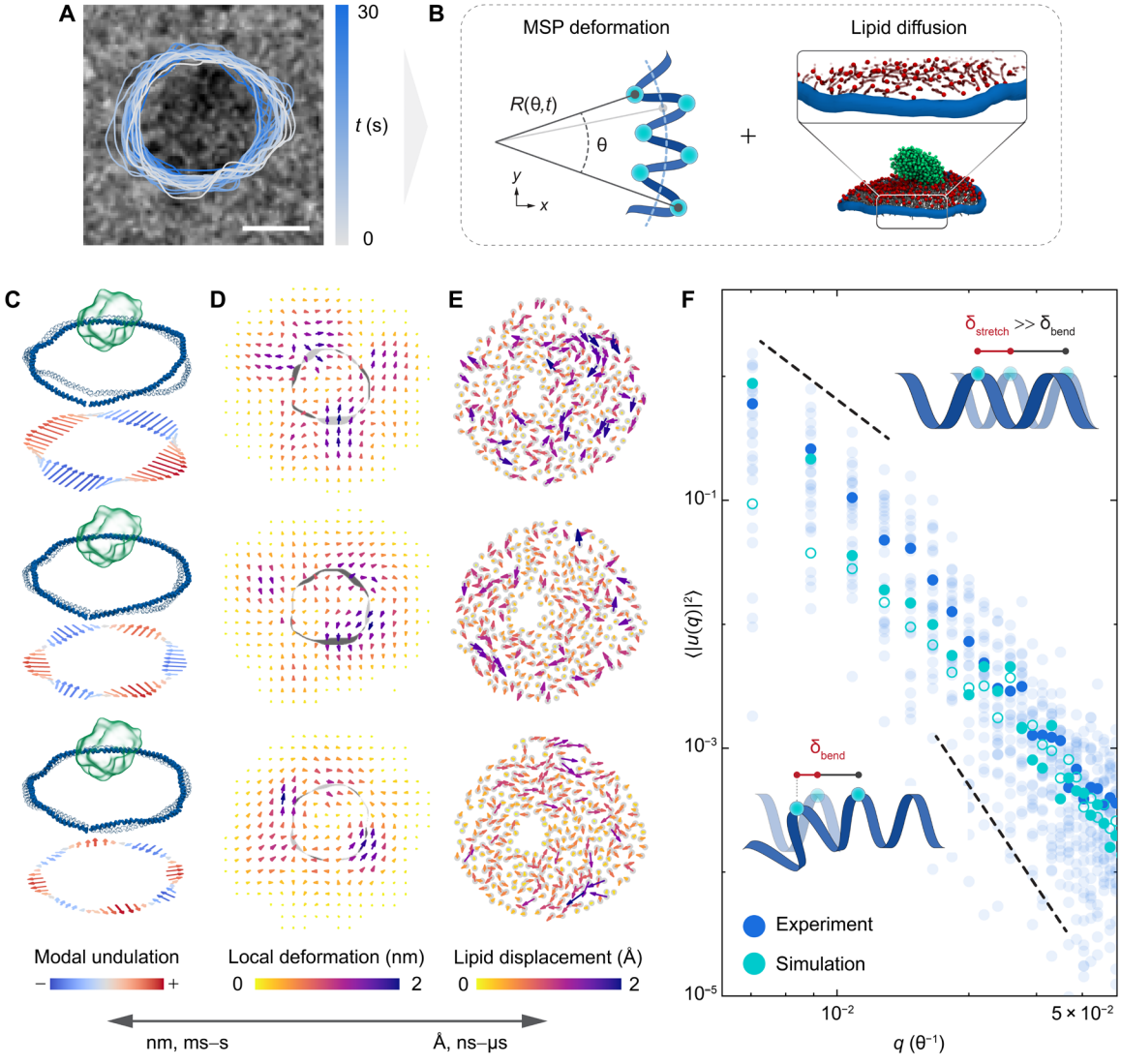

Fig. 3. Nanodisc fluctuations as "fingerprints" of molecular phenomena. (**A**) Nanodisc undulations (highlighted with overlaid contours from different time points) involve two components: (**B**) fluctuations of the MSPs, based on a balance between thermal energy and molecular mechanics, and fluid-like diffusion of interior lipids. (**C**) A normal mode analysis of the MD simulations shows that undulations decompose into principally elliptical deformations (56%), with gradually lesser contributions from third-order (22%), fourth-order (6%), and higher-order radial modes (collectively, 16%). These mechanics are coupled to motion of lipids in the nanodisc interior, which can be measured (**D**) on a "continuum" level, as an overall deformation vector field from the experimental data or (**E**) on the molecular level, following displacements of individual lipid molecules, from MD simulations. Individual panels are examples of this "flow" between experimental (D) and simulation (E) frames. Between experiment and simulation, these measurements span from nanometers and milliseconds to angstroms and nanoseconds. (**F**) Fourier analysis of nanodisc fluctuations suggests that tension dominates at relatively large scales ($\delta_{stretch}$), whereas bending rigidity dominates at smaller scales (δ_{bend}). The simulation data in solid circles corresponds to results from nanodiscs containing CYP2J2, and the data in open circles corresponds to nanodiscs with CYP3A4. Scale bar, 10 nm.

Over the seconds to minute timeframe of our observations, we occasionally captured an unexpected and more extensive form of fluctuation (Fig. 4, A and B, and movie S3), in which nanodiscs would "stretch" or "finger" to form distinct domains interdigitated with concave regions (Fig. 4, A to D, and figs. S22 and 23). These extended deformations were not observed in MD simulations, from the perspective of which they are rare events, but appeared in approximately a third of the high-quality movies (movies lacking obvious electron beam effects) of large nanodiscs and lasted a few tens of seconds. We differentiate fingering from normal undulations based on the contour circularity, a measure of "convexness" (circularities <0.8 were associated with fingering; fig. S22). Fingering also converts a nanodisc described by a single, large domain into one composed of multiple zones approaching 4 to 5 nm. Unexpectedly, filled nanodiscs that experienced fingering fluctuations eventually regained their overall round shape (fig. S23 and movie S3). When this occurred, the projected area and perimeter of the nanodisc before and after fingering were within ~8% of each other (fig. S23, A and B), suggesting minimal damage or mass loss. Fingering nanodiscs also retained a major domain (described by the maximum inscribed circle, with size d_{insc}) of at least ~12 nm (Fig. 4, C and D) despite their large overall distortion. In contrast, when

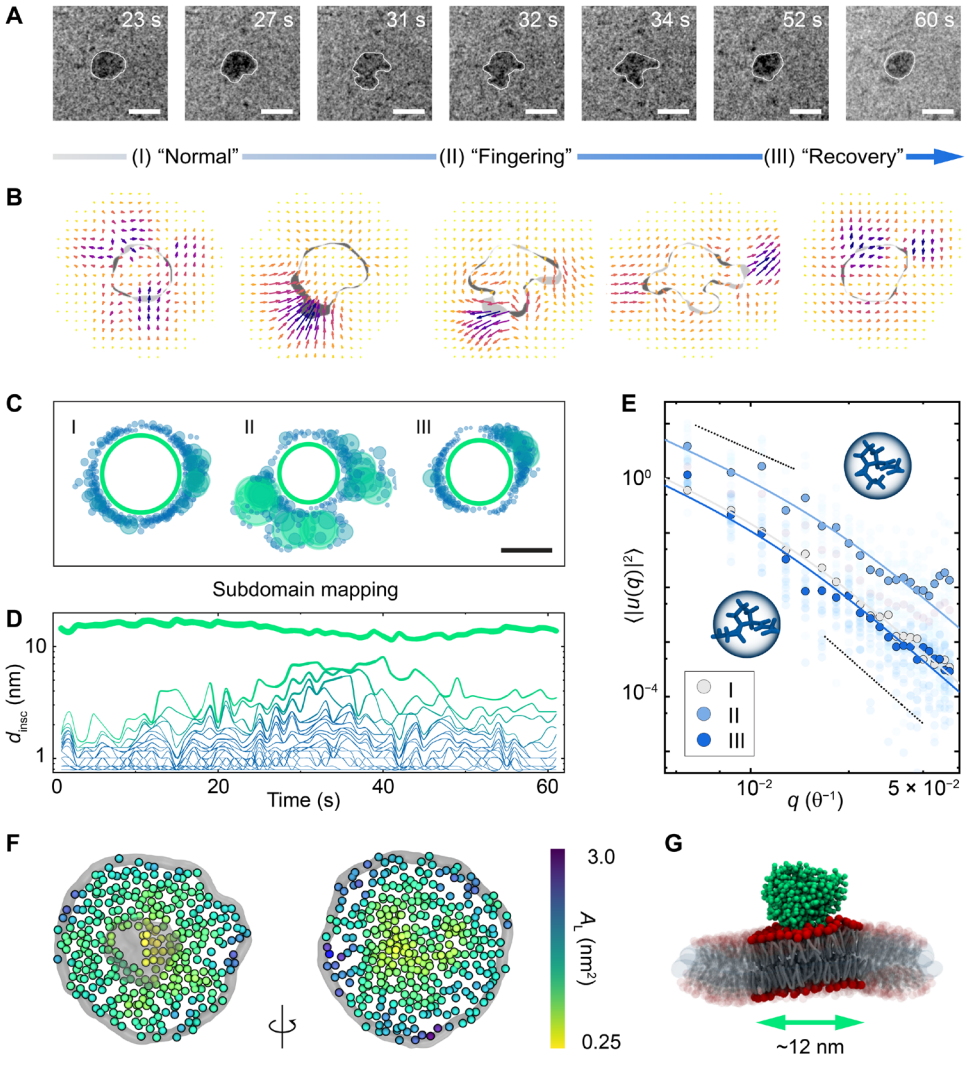

Fig. 4. Fingering fluctuations and the role of lipid–protein interactions. (**A**) Representative experimental snapshots of nanodiscs contorted into complex shapes, involving more drastic mass transport (**B**) and the formation of extended concave regions. The reduced visibility of CYP2J2 in these snapshots may in part be attributed to greater motion blur during vigorous fingering fluctuations. (**C** and **D**) Fingering converts the nanodisc from a shape that can be mostly described by a single, large domain into one that requires several zones (fig. S25; different colors denote different zones) approaching 4 to 5 nm in diameter. However, the largest domain consistently exceeds 12 nm in diameter. (**E**) Tension-dominated and bending-dominated fluctuation regimes are present before (I), during (II), and after (III) fingering, and the mechanics of the contour appear qualitatively recovered in (III). (**F**) Recovery processes may be facilitated by lipid–protein interactions, which lead to altered packing (area-per-lipid, A_L) in the vicinity of the membrane protein, as revealed by MD simulations. (**G**) This altered packing defines a zone of the nanodisc (marked by the green arrow) that may be preserved even during extensive perturbations. Scale bars, 20 nm (A) and 15 nm (C).

empty nanodiscs experienced fingering fluctuations, domains decreased to ~5 nm before complete disintegration (fig. S23C and movie S3). Together, (i) filled nanodiscs but not empty ones can recover from fingering fluctuations and (ii) recovery may be facilitated by a central core.

Recovered nanodiscs regain not only their size and shape but also their interfacial mechanics, suggesting that fingering is related to a reversible molecular phenomenon. Specifically, while $\langle|u(q)|^2\rangle$ increases by ~20% during fingering fluctuations (Fig. 4E, regime II), tension- and rigidity-dominated regimes are preserved. After fingering, the mechanics of the nanodisc contour are, within experimental error, restored (Fig. 4E, regime I versus regime III, and table S4), suggesting their structural integrity. Fingering fluctuations may therefore depend on a process such as bending at the prolines that punctuate MSP helices. Note that prolines also explain why the nanodisc interface appears much more flexible than a contiguous α helix (*47*). On ~10^1-s scales, prolines can reversibly isomerize (*48*), which would change local bending angles in the MSP (movie S3), and the morphology of fingering nanodiscs is consistent with the "geometry" of the proline distribution (fig. S24). Such a process is thought to occur in structural transitions of lipoprotein particles (*49*), from which MSPs are derived, but has not been reported in nanodiscs, although an (unknown) extended conformational transition occurring over seconds has been suggested (*50*). The large energetic barrier (~20 kcal/mol) and corresponding time scales associated with this process may explain why fingering was not observed in MD simulations, without

introducing forces to bias the system (*51*). At the same time, this underscores a complementary nature of liquid phase TEM: to detect phenomena that, to MD simulations, are rare events but still at "single-particle" resolution.

The fact that empty nanodiscs do not recover from fingering highlights the impact of a membrane protein not only on overall nanodisc shape fluctuations (Fig. 2E and fig. S15) but also on nanodisc stability, as a consequence of lipid–protein interactions (Fig. 2D). Even when filled nanodiscs finger, the preserved ~12-nm domain is large enough to harbor CYP2J2 and 2 to 3 nm of intervening lipids (Fig. 4, F and G). In addition, recovery generally occurs around this region (Fig. 4C). MD simulations indicate that the lipids near the protein are packed more densely (Fig. 4F and fig. S26), a trait that spans to the bottom leaflet of the nanodisc that is not in contact with a membrane protein. The membrane near the protein is also compacted in the *z* direction (fig. S26). Together, these observations suggest that the influence of lipid–membrane protein interactions reaches not just across the few innermost annular lipid shells from where the protein is inserted but 3 to 4 nm from the periphery of the protein (Fig. 4G). The structurally and dynamically modified zone delineated by these interactions may protect against extensive perturbations. Because empty nanodiscs lack this region, such a relatively stable domain may not exist and, given the liquid-like nature of the lipids used here, extensive fluctuations are irrevocable (movie S4 and fig. S23). While 10^1- to 10^2-nm membrane islands are believed to be present in biological membranes (*27*), experimental characterization of their dynamics on such a length scale, and particularly their role in structural stability, has been challenging. We are hopeful that present and future insight from molecular videography will help understand these and related biophysical phenomena even in macroscopic biological membranes.

DISCUSSION

Our results show how biophysical insight can be obtained through direct, experimental observation of biomolecular dynamics in liquid at the nanometer scale. Nanodisc dynamics in particular reveal "fingerprints" of lipid–protein interactions, inviting future studies aimed at understanding the roles of lipid composition and phase behavior, and their interplay with membrane protein structure. Of particular interest will be studies controlling the liquid chamber environment in situ, with temperature, electric fields, etc. In addition, extending our use of molecular modeling and simulation to infer submolecular-scale information from single snapshots could push the effective resolution of electron videography even further in the future. More generally, we expect the technical and analytical approaches described here can be extended to study not only a wide range of nanodiscs—with variable lipid and protein composition—but also to a broad spectrum of (bio)molecular assemblies.

The combination of low dose-rate imaging and graphene encapsulation appears to be critical to the success of these studies. Here, we have provided evidence that encapsulated biomolecules can remain sufficiently intact at least so as to present the expected shape, size, contrast, and certain fluctuations for extended periods. At the resolution obtained so far, intramolecular dynamics before the onset of visible damage quantitatively match those observed in MD simulations where the electron beam and substrate effects are not present (text S3). We hope these promising, initial results encourage the substantial future work necessary to pinpoint specific mechanisms, whereby, for example, graphene or other "scavengers" could elicit these protective effects (text S1). These questions present a tremendous challenge but are rooted in important areas of basic science. Other enduring challenges are associated with our relatively low temporal resolution (millisecond to second) compared to many biomolecular phenomena and information lost to diffusive and intramolecular motion. Even with the advent of faster and faster electron detectors, one must begin to consider the balance between dose per frame and dose per second in terms of sample stability; although the stability limit may be defined by the dose over time, the ultimate interpretability limit may be defined by dose per frame. In general, the final spatial resolution here and in the future can be expected to be a mixture of both "optical" and "dynamic" effects, with the fastest processes corresponding to the smallest length scales more likely to be smoothed out over a given exposure. Here, we expect that the experimentally measured resolution comprises both these effects and any contribution from the image processing pipeline (text S8). Nevertheless, with parallel technical improvements in sample preparation and video analysis that integrate machine intelligence (*52*), for example, we hope to push closer to the direct observation of proteins and other biomolecules "in action" when performing functional physical or chemical tasks and establish a sister to cryogenic TEM in the study of molecular biophysics.

MATERIALS AND METHODS

Materials

Ammonium persulfate [$(NH_4)_2S_2O_8$, >98.0%], ammonium molybdate [$(NH_4)_2MoO_4$, 99.98%, trace metals basis], D-(+)-trehalose dihydrate ($C_{12}H_{22}O_{11}{\cdot}2H_2O$, ≥99.0%), Amberlite beads (product XAD-2), β-mercaptoethanol ($HOCH_2CH_2SH$, for molecular biology, 99%), sodium chloride (NaCl, anhydrous, ACS reagent, ≥99%), and potassium chloride (KCl, BioReagent, ≥99.0%) were purchased from Sigma-Aldrich. Potassium phosphate dibasic (HK_2PO_4, ≥98%), potassium phosphate monobasic (H_2KPO_4, ≥99.0%), imidazole (for molecular biology, BP305-50), glycerol (for molecular biology), and materials for Luria Bertani (LB) medium and Terrific Broth [Bacto peptone (211677), tryptone (BP1421-500), Bacto yeast extract (212720), and Bacto agar (214010)] were purchased from Thermo Fisher Scientific. Magnesium chloride (MgCl, product 0288) was purchased from VWR. Adenosine-5′-triphosphate disodium salt trihydrate (ATP, ≥98%) was purchased from Chem Impex International Inc. Triton X-100 {2-[4-(2,4,4-trimethylpentan-2-yl)phenoxy]ethanol, product BP151-500} was purchased from Fisher BioReagents. DNase I (from bovine pancreas, D-300-500), chloramphenicol (USP grade, C-105-100), ampicillin (USP grade, A-301-100), kanamycin monosulfate (USP grade, K-120-25), L-arabinose (A-300-1), isopropyl-β-D-thiogalactopyranoside (I2481C-25), and phenylmethylsulfonyl fluoride (P-470-25) were purchased from GoldBio. δ-aminolevulinic acid (5-amino-4-oxopentanoic acid, A167) was purchased from Frontier Scientific. POPC (1-palmitoyl-2-oleoyl-sn-glycero-3-phosphocholine) in chloroform was purchased from Avanti Polar Lipids. Electron microscopy grids with either a uniform carbon film and 400-mesh copper support (CF400-Cu) or a Quantifoil carbon film and 300-mesh gold support (Q325AR-14 or Q3100AR1.3) were obtained from Electron Microscopy Sciences. Few-layer graphene (three to five layers) prepared by chemical vapor deposition (CVD) on copper foil (product CVCU3042) was obtained from ACS Material. All experiments used ultrapure water (18.2 megohm·cm at 25°C) from a Milli-Q Advantage A10 system.

Nanodisc preparation

CYP2J2 and MSPs were expressed and purified following protocols described in (*34*). Recombinant human Δ34-CYP2J2 was expressed in DH5α *Escherichia coli* cells, which were grown in Terrific Broth to an optical density of 1.0 before inducing CYP2J2 expression. Membrane fractions were then harvested by centrifugation, and protein content was extracted by adding cholate, followed by additional centrifugation. CYP2J2 was then isolated on a nickel–nitrilotriacetic acid (Ni-NTA) affinity column before being eluted at a concentration of ~150 nM using imidazole. MSPs were also expressed in *E. coli*, grown in Luria Bertrani medium containing kanamycin. Following expression, cells were resuspended in potassium phosphate buffer containing Triton X-100 before sonication and centrifugation. The supernatant was also passed through a Ni–NTA column, and MSPs were eluted using imidazole, which was removed by dialysis.

Nanodiscs were assembled as described in our previous work (*34*). POPC stocks in chloroform were dried under a stream of N_2 gas before being reconstituted in potassium phosphate buffer (0.1 M, pH 7.4). For large nanodiscs, purified MSP 2N2 was added in a lipid-to-MSP molar ratio of 239:1, followed by purified CYP2J2 in a CYP2J2-to-MSP molar ratio of 2:1. Small nanodiscs were prepared by adding MSP 1E3D1 in a lipid-to-MSP ratio of 130:1 and CYP2J2 in a CYP2J2-to-MSP ratio of 1:10. Nanodisc assembly was induced by gradual extraction of cholate, through incubation with Amberlite beads. Filled or empty nanodiscs were then purified by size exclusion chromatography, with filled nanodiscs being identified on the basis of absorbance at 417 nm (characteristic of the heme in CYP2J2). For additional details on preparation and purification of nanodiscs, see text S5.

Electron microscopy

Micrographs of negatively stained nanodiscs were collected on a JEOL 2100 TEM operating at 80 kV using ammonium molybdate as the contrast-enhancing agent. Liquid phase TEM was performed using graphene liquid chambers in the "channel" configuration, made via a wet-transfer, polymer-free method. Gold mesh Quantifoil grids with a holey carbon film were adhered to CVD graphene on copper foil by adding a small amount of isopropanol to the surface of the graphene, allowing the solvent to diffuse beneath the grids and then dry in air. The copper film bearing the graphene was then etched away on the surface of an ammonium persulfate solution. Intervening graphene was removed, and the grids were rinsed on three large water baths and laid to dry on a clean fiber cloth. In parallel, the copper from another sheet of CVD graphene without adhered grids was etched on an ammonium persulfate solution before serial dilution of the solution to remove etching by-products. A ~0.1-μL droplet of the nanodisc suspension was then dispensed onto a graphene-coated grid, which was inverted over the freely floating graphene and gently rested on top. After leaving the grid and graphene for a few minutes to form a seal, the whole assembly was gently scooped from the water surface, allowed to dry briefly in air, and inserted into the microscope for imaging. Movies were collected on a JEOL 2100 TEM with an accelerating voltage of 200 kV and low dose rates (generally less than 10 $e^- Å^{-2} s^{-1}$), measured based on blank-image intensity calibration with a custom-designed, Faraday cup holder. Frames with an exposure time of 0.3 s were collected every 1 s with a total dose, depending on the duration of the movie, of ~10^3 $e^- Å^{-2}$. For additional details on electron microscopy sample preparation and experiments, please see text S6. Movie and image processing methods are described in detail in text S7. Aspects of imaging resolution are discussed in text S8.

MD and image simulations

Coarse-grained models of large and small, filled and unfilled nanodiscs were assembled using the CHARMM-GUI interface and parameterized using MARTINI 2.2 (for amino acid beads) or MARTINI 2.0 (for lipid beads). All MD simulations—including minimization and equilibration—were performed in GROMACS 5.0. Production runs were performed for 100,000,000 steps (2 μs) in increments of 20 fs. For image simulations, select frames from the coarse-grained simulation were back-mapped to atomistic representations using the MARTINI all-atom converter. Image simulations were then conducted using the resulting atomic coordinates and on the basis of contrast transfer theory using functions from the SPIDER software package. For additional details on model building, simulation protocols, and the analysis of simulation trajectories, please see texts S9 and S10.

Supplementary Materials

This PDF file includes:

Text S1 to S10
Figs. S1 to S26
Tables S1 to S4
Legends for movies S1 to S4
References

Other Supplementary Material for this manuscript includes the following:

Movies S1 to S4

REFERENCES AND NOTES

1. R. Zhou, X. Huang, C. J. Margulis, B. J. Berne, Hydrophobic collapse in multidomain protein folding. *Science* **305**, 1605–1609 (2004).
2. P. Ball, Water as an active constituent in cell biology. *Chem. Rev.* **108**, 74–108 (2008).
3. M. Chaplin, Do we underestimate the importance of water in cell biology? *Nat. Rev. Mol. Cell Biol.* **7**, 861–866 (2006).
4. T. Bengtsen, V. L. Holm, L. R. Kjølbye, S. R. Midtgaard, N. T. Johansen, G. Tesei, S. Bottaro, B. Schiøtt, L. Arleth, K. Lindorff-Larsen, Structure and dynamics of a nanodisc by integrating NMR, SAXS and SANS experiments with molecular dynamics simulations. *eLife* **9**, 1 (2020).
5. M. Hong, Y. Zhang, F. Hu, Membrane protein structure and dynamics from NMR spectroscopy. *Annu. Rev. Phys. Chem.* **63**, 1–24 (2012).
6. A. B. Marciel, S. Srivastava, J. M. Ting, M. V. Tirrell, "Chapter Eight - SAXS methods for investigating macromolecular and self-assembled polyelectrolyte complexes" in *Methods in Enzymology*, C. D. Keating, Ed. (Academic Press, 2021), vol. 646, pp. 223–259.
7. F. M. Ross, Opportunities and challenges in liquid cell electron microscopy. *Science* **350**, (2015).
8. T. Nakane, A. Kotecha, A. Sente, G. McMullan, S. Masiulis, P. M. G. E. Brown, I. T. Grigoras, L. Malinauskaite, T. Malinauskas, J. Miehling, T. Uchański, L. Yu, D. Karia, E. V. Pechnikova, E. de Jong, J. Keizer, M. Bischoff, J. McCormack, P. Tiemeijer, S. W. Hardwick, D. Y. Chirgadze, G. Murshudov, A. R. Aricescu, S. H. W. Scheres, Single-particle cryo-EM at atomic resolution. *Nature* **587**, 152–156 (2020).
9. N. Kodera, D. Yamamoto, R. Ishikawa, T. Ando, Video imaging of walking myosin V by high-speed atomic force microscopy. *Nature* **468**, 72–76 (2010).
10. F. Balzarotti, Y. Eilers, K. C. Gwosch, A. H. Gynnå, V. Westphal, F. D. Stefani, J. Elf, S. W. Hell, Nanometer resolution imaging and tracking of fluorescent molecules with minimal photon fluxes. *Science* **355**, 606–612 (2017).
11. E. Betzig, G. H. Patterson, R. Sougrat, O. W. Lindwasser, S. Olenych, J. S. Bonifacino, M. W. Davidson, J. Lippincott-Schwartz, H. F. Hess, Imaging intracellular fluorescent proteins at nanometer resolution. *Science* **313**, 1642–1645 (2006).
12. K. M. Yip, N. Fischer, E. Paknia, A. Chari, H. Stark, Atomic-resolution protein structure determination by cryo-EM. *Nature* **587**, 157–161 (2020).
13. S. Huaizong, W. Liu Dongliang, L. J. Kun, Y. Nieng, Structures of human Nav1.7 channel in complex with auxiliary subunits and animal toxins. *Science* **363**, 1303–1308 (2019).

14. X. Ye, M. R. Jones, L. B. Frechette, Q. Chen, A. S. Powers, P. Ercius, G. Dunn, G. M. Rotskoff, S. C. Nguyen, V. P. Adiga, A. Zettl, E. Rabani, P. L. Geissler, A. P. Alivisatos, Single-particle mapping of nonequilibrium nanocrystal transformations. *Science* **354**, 874–877 (2016).
15. J. Park, H. Elmlund, P. Ercius, J. M. Yuk, D. T. Limmer, Q. Chen, K. Kim, S. H. Han, D. A. Weitz, A. Zettl, A. P. Alivisatos, 3D structure of individual nanocrystals in solution by electron microscopy. *Science* **349**, 290–295 (2015).
16. Z. Ou, Z. Wang, B. Luo, E. Luijten, Q. Chen, Kinetic pathways of crystallization at the nanoscale. *Nat. Mater.* **19**, 450–455 (2020).
17. A. Ianiro, H. Wu, M. M. J. van Rijt, M. P. Vena, A. D. A. Keizer, A. C. C. Esteves, R. Tuinier, H. Friedrich, N. A. J. M. Sommerdijk, J. P. Patterson, Liquid–liquid phase separation during amphiphilic self-assembly. *Nat. Chem.* **11**, 320–328 (2019).
18. A. C. Varano, A. Rahimi, M. J. Dukes, S. Poelzing, S. M. McDonald, D. F. Kelly, Visualizing virus particle mobility in liquid at the nanoscale. *Chem. Commun.* **51**, 16176–16179 (2015).
19. U. M. Mirsaidov, H. Zheng, Y. Casana, P. Matsudaira, Imaging protein structure in water at 2.7 nm resolution by transmission electron microscopy. *Biophys. J.* **102**, L15–L17 (2012).
20. S. Keskin, N. de Jonge, Reduced radiation damage in transmission electron microscopy of proteins in graphene liquid cells. *Nano Lett.* **18**, 7435–7440 (2018).
21. N. de Jonge, D. B. Peckys, G. J. Kremers, D. W. Piston, Electron microscopy of whole cells in liquid with nanometer resolution. *Proc. Natl. Acad. Sci. U.S.A.* **106**, 2159–2164 (2009).
22. H. Cho, M. R. Jones, S. C. Nguyen, M. R. Hauwiller, A. Zettl, A. P. Alivisatos, The use of graphene and its derivatives for liquid-phase transmission electron microscopy of radiation-sensitive specimens. *Nano Lett.* **17**, 414–420 (2017).
23. M. P. Muller, T. Jiang, C. Sun, M. Lihan, S. Pant, P. Mahinthichaichan, A. Trifan, E. Tajkhorshid, Characterization of lipid–protein interactions and lipid-mediated modulation of membrane protein function through molecular simulation. *Chem. Rev.* **119**, 6086–6161 (2019).
24. E. G. Brandt, A. R. Braun, J. N. Sachs, J. F. Nagle, O. Edholm, Interpretation of fluctuation spectra in lipid bilayer simulations. *Biophys. J.* **100**, 2104–2111 (2011).
25. Y. Gao, E. Cao, D. Julius, Y. Cheng, TRPV1 structures in nanodiscs reveal mechanisms of ligand and lipid action. *Nature* **534**, 347–351 (2016).
26. I. G. Denisov, S. G. Sligar, Nanodiscs in membrane biochemistry and biophysics. *Chem. Rev.* **117**, 4669–4713 (2017).
27. E. Sezgin, I. Levental, S. Mayor, C. Eggeling, The mystery of membrane organization: Composition, regulation and roles of lipid rafts. *Nat. Rev. Mol. Cell Biol.* **18**, 361–374 (2017).
28. R. Phillips, T. Ursell, P. Wiggins, P. Sens, Emerging roles for lipids in shaping membrane-protein function. *Nature* **459**, 379–385 (2009).
29. D. Martinez, M. Decossas, J. Kowal, L. Frey, H. Stahlberg, E. J. Dufourc, R. Riek, B. Habenstein, S. Bibow, A. Loquet, Lipid membrane biochemistry and biophysics. *ChemPhysChem* **18**, 2651–2657 (2017).
30. Y. Li, A. Z. Kijac, S. G. Sligar, C. M. Rienstra, Structural analysis of nanoscale self-assembled discoidal lipid bilayers by solid-state NMR spectroscopy. *Biophys. J.* **91**, 3819–3828 (2006).
31. B. I. Sejdiu, D. P. Tieleman, Lipid-protein interactions are a unique property and defining feature of G protein-coupled receptors. *Biophys. J.* **118**, 1887–1900 (2020).
32. A. Y. Shih, I. G. Denisov, J. C. Phillips, S. G. Sligar, K. Schulten, Molecular dynamics simulations of discoidal bilayers assembled from truncated human lipoproteins. *Biophys. J.* **88**, 548–556 (2005).
33. Y. V. Grinkova, I. G. Denisov, S. G. Sligar, Engineering extended membrane scaffold proteins for self-assembly of soluble nanoscale lipid bilayers. *Protein Eng. Des. Sel.* **23**, 843–848 (2010).
34. L. N. Carnevale, A. S. Arango, W. R. Arnold, E. Tajkhorshid, A. Das, Endocannabinoid virodhamine is an endogenous inhibitor of human cardiovascular CYP2J2 epoxygenase. *Biochemistry* **57**, 6489–6499 (2018).
35. K. H. Nagamanasa, H. Wang, S. Granick, Liquid-cell electron microscopy of adsorbed polymers. *Adv. Mater.* **29**, 1703555 (2017).
36. H. Wang, K. H. Nagamanasa, Y.-J. Kim, O.-H. Kwon, S. Granick, Longer-lasting electron-based microscopy of single molecules in aqueous medium. *ACS Nano* **12**, 8572–8578 (2018).
37. I. Casuso, J. Khao, M. Chami, P. Paul-Gilloteaux, M. Husain, J.-P. Duneau, H. Stahlberg, J. N. Sturgis, S. Scheuring, Characterization of the motion of membrane proteins using high-speed atomic force microscopy. *Nat. Nanotechnol.* **7**, 525–529 (2012).
38. M. Przybylo, J. Sýkora, J. Humpolíčková, A. Benda, A. Zan, M. Hof, Lipid diffusion in giant unilamellar vesicles Is more than 2 times faster than in supported phospholipid bilayers under identical conditions. *Langmuir* **22**, 9096–9099 (2006).
39. M. Rose, N. Hirmiz, J. M. Moran-Mirabal, C. Fradin, Lipid diffusion in supported lipid bilayers: A comparison between line-scanning fluorescence correlation spectroscopy and single-particle tracking. *Membranes* **5**, 702–721 (2015).
40. C. Scomparin, S. Lecuyer, M. Ferreira, T. Charitat, B. Tinland, Diffusion in supported lipid bilayers: Influence of substrate and preparation technique on the internal dynamics. *Eur. Phys. J. E* **28**, 211–220 (2009).
41. E. L. Florin, H. E. Gaub, Painted supported lipid membranes. *Biophys. J.* **64**, 375–383 (1993).
42. A. W. Shaw, V. S. Pureza, S. G. Sligar, J. H. Morrissey, The local phospholipid environment modulates the activation of blood clotting. *J. Biol. Chem.* **282**, 6556–6563 (2007).
43. S. Orioli, C. G. Henning Hansen, L., Ab initiodetermination of the shape of membrane proteins in a nanodisc. *Acta Crystallogr. Sect. D* **77**, 176–193 (2021).
44. M. B. Stone, S. A. Shelby, S. L. Veatch, Super-resolution microscopy: Shedding light on the cellular plasma membrane. *Chem. Rev.* **117**, 7457–7477 (2017).
45. L. Zhang, H. Tong, M. Garewal, G. Ren, Optimized negative-staining electron microscopy for lipoprotein studies. *Biochim. Biophys. Acta* **1830**, 2150–2159 (2013).
46. C. Gan, M. Ao, Z. Liu, Y. Chen, Imaging and force measurement of LDL and HDL by AFM in air and liquid. *FEBS Open Bio* **5**, 276–282 (2015).
47. S. Choe, S. X. Sun, The elasticity of α-helices. *J. Chem. Phys.* **122**, 244912 (2005).
48. S. Osváth, M. Gruebele, Proline can have opposite effects on fast and slow protein folding phases. *Biophys. J.* **85**, 1215–1222 (2003).
49. D. W. Borhani, D. P. Rogers, J. A. Engler, C. G. Brouillette, Crystal structure of truncated human apolipoprotein A-I suggests a lipid-bound conformation. *Proc. Natl. Acad. Sci. U.S.A.* **94**, 12291–12296 (1997).
50. C. R. Morgan, C. M. Hebling, K. D. Rand, D. W. Stafford, J. W. Jorgenson, J. R. Engen, Conformational transitions in the membrane scaffold protein of phospholipid bilayer nanodiscs. *Mol. Cell. Proteomics* **10**, 010876 (2011).
51. D. Hamelberg, T. Shen, J. A. McCammon, Phosphorylation effects on cis/trans isomerization and the backbone conformation of serine−proline motifs: Accelerated molecular dynamics analysis. *J. Am. Chem. Soc.* **127**, 1969–1974 (2005).
52. L. Yao, Z. Ou, B. Luo, C. Xu, Q. Chen, Machine learning to reveal nanoparticle dynamics from liquid-phase TEM videos. *ACS Cent. Sci.* **6**, 1421–1430 (2020).
53. R. F. Egerton, Mechanisms of radiation damage in beam-sensitive specimens, for TEM accelerating voltages between 10 and 300 kV. *Microsc. Res. Tech.* **75**, 1550–1556 (2012).
54. R. F. Egerton, P. Li, M. Malac, Radiation damage in the TEM and SEM. *Micron* **35**, 399–409 (2004).
55. J. W. Smith, Q. Chen, Liquid-phase electron microscopy imaging of cellular and biomolecular systems. *J. Mater. Chem. B* **8**, 8490–8506 (2020).
56. N. M. Schneider, M. M. Norton, B. J. Mendel, J. M. Grogan, F. M. Ross, H. H. Bau, Electron–water interactions and implications for liquid cell electron microscopy. *J. Phys. Chem. C* **118**, 22373–22382 (2014).
57. T. J. Woehl, P. Abellan, Defining the radiation chemistry during liquid cell electron microscopy to enable visualization of nanomaterial growth and degradation dynamics. *J. Microsc.* **265**, 135–147 (2017).
58. M. R. Hauwiller, J. C. Ondry, C. M. Chan, P. Khandekar, J. Yu, A. P. Alivisatos, Gold nanocrystal etching as a means of probing the dynamic chemical environment in graphene liquid cell electron microscopy. *J. Am. Chem. Soc.* **141**, 4428–4437 (2019).
59. M. R. Hauwiller, L. B. Frechette, M. R. Jones, J. C. Ondry, G. M. Rotskoff, P. Geissler, A. P. Alivisatos, Unraveling kinetically-driven mechanisms of gold nanocrystal shape transformations using graphene liquid cell electron microscopy. *Nano Lett.* **18**, 5731–5737 (2018).
60. M. R. Hauwiller, X. Ye, M. R. Jones, C. M. Chan, J. J. Calvin, M. F. Crook, H. Zheng, A. P. Alivisatos, Tracking the effects of ligands on oxidative etching of gold nanorods in graphene liquid cell electron microscopy. *ACS Nano* **14**, 10239–10250 (2020).
61. T. Gupta, N. M. Schneider, J. H. Park, D. Steingart, F. M. Ross, Spatially dependent dose rate in liquid cell transmission electron microscopy. *Nanoscale* **10**, 7702–7710 (2018).
62. J. Kim, M. R. Jones, Z. Ou, Q. Chen, In situ electron microscopy imaging and quantitative structural modulation of nanoparticle superlattices. *ACS Nano* **10**, 9801–9808 (2016).
63. J. M. Grogan, N. M. Schneider, F. M. Ross, H. H. Bau, Bubble and pattern formation in liquid induced by an electron beam. *Nano Lett.* **14**, 359–364 (2014).
64. H. Zheng, S. A. Claridge, A. M. Minor, A. P. Alivisatos, U. Dahmen, Nanocrystal diffusion in a liquid thin film observed by in situ transmission electron microscopy. *Nano Lett.* **9**, 2460–2465 (2009).
65. J. M. Yuk, J. Park, P. Ercius, K. Kim, D. J. Hellebusch, M. F. Crommie, J. Y. Lee, A. Zettl, A. P. Alivisatos, High-resolution EM of colloidal nanocrystal growth using graphene liquid cells. *Science* **336**, 61–64 (2012).
66. Z. Ou, C. Liu, L. Yao, Q. Chen, Nanoscale cinematography of Soft Matter system under liquid-phase TEM. *Acc. Mater. Res.* **1**, 41–52 (2020).
67. R. E. Robberstad Møller-Nilsen, S. Canepa, E. Jensen, H. Sun, I. A. Moreno-Hernandez, M. N. Yesibolati, A. P. Alivisatos, K. S. Mølhave, Quantifying aqueous radiolytic products in liquid phase electron microscopy. *J. Phys. Chem. C* **127**, 15512–15522 (2023).
68. B. Fritsch, P. Malgaretti, J. Harting, K. J. J. Mayrhofer, A. Hutzler, Precision of radiation chemistry networks: Playing Jenga with kinetic models for liquid-phase electron microscopy. *Precis. Chem.* **1**, 592–601 (2023).
69. B. Fritsch, T. S. Zech, M. P. Bruns, A. Körner, S. Khadivianazar, M. Wu, N. Zargar Talebi, S. Virtanen, T. Unruh, M. P. M. Jank, E. Spiecker, A. Hutzler, Radiolysis-driven evolution of gold nanostructures—Model verification by scale bridging in situ liquid-phase transmission electron microscopy and x-ray diffraction. *Adv. Sci.* **9**, 2202803 (2022).

70. M. F. Crook, I. A. Moreno-Hernandez, J. C. Ondry, J. Ciston, K. C. Bustillo, A. Vargas, A. P. Alivisatos, EELS studies of cerium electrolyte reveal substantial solute concentration effects in graphene liquid cells. *J. Am. Chem. Soc.* **145**, 6648–6657 (2023).
71. T. Couasnon, B. Fritsch, M. P. M. Jank, R. Blukis, A. Hutzler, L. G. Benning, Goethite mineral dissolution to probe the chemistry of radiolytic water in liquid-phase transmission electron microscopy. *Adv. Sci.* **10**, 2301904 (2023).
72. Q. Chen, J. M. Smith, J. Park, K. Kim, D. Ho, H. I. Rasool, A. Zettl, A. P. Alivisatos, 3D motion of DNA-Au nanoconjugates in graphene liquid cell electron microscopy. *Nano Lett.* **13**, 4556–4561 (2013).
73. H. Wang, B. Li, Y.-J. Kim, O.-H. Kwon, S. Granick, Intermediate states of molecular self-assembly from liquid-cell electron microscopy. *Proc. Natl. Acad. Sci. U.S.A.* **117**, 1283–1292 (2020).
74. B. Janicek, P. Kharel, S. hyun Bae, P. Huang, Understanding graphene's role as a protective substrate for atomic-resolution electron microscopy of small organic molecules. *Microsc. Microanal.* **27**, 2900–2901 (2021).
75. G. Algara-Siller, S. Kurasch, M. Sedighi, O. Lehtinen, U. Kaiser, The pristine atomic structure of MoS2 monolayer protected from electron radiation damage by graphene. *Appl. Phys. Lett.* **103**, 203107 (2013).
76. C. J. Russo, L. A. Passmore, Controlling protein adsorption on graphene for cryo-EM using low-energy hydrogen plasmas. *Nat. Methods* **11**, 649–652 (2014).
77. C. J. Russo, L. A. Passmore, Progress towards an optimal specimen support for electron cryomicroscopy. *Curr. Opin. Struct. Biol.* **37**, 81–89 (2016).
78. D. T. Gillespie, Stochastic simulation of chemical kinetics. *Annu. Rev. Phys. Chem.* **58**, 35–55 (2007).
79. D. T. Gillespie, Exact stochastic simulation of coupled chemical reactions. *J. Phys. Chem.* **81**, 2340–2361 (1977).
80. D. J. Warne, R. E. Baker, M. J. Simpson, Simulation and inference algorithms for stochastic biochemical reaction networks: From basic concepts to state-of-the-art. *J. R. Soc. Interface* **16**, 20180943 (2019).
81. V. Georgakilas, J. N. Tiwari, K. C. Kemp, J. A. Perman, A. B. Bourlinos, K. S. Kim, R. Zboril, Noncovalent functionalization of graphene and graphene oxide for energy materials, biosensing, catalytic, and biomedical applications. *Chem. Rev.* **116**, 5464–5519 (2016).
82. J. S. Park, N.-I. Goo, D.-E. Kim, Mechanism of DNA adsorption and desorption on graphene oxide. *Langmuir* **30**, 12587–12595 (2014).
83. S. Granick, Motions and relaxations of confined liquids. *Science* **253**, 1374–1379 (1991).
84. K. Takamura, H. Fischer, N. R. Morrow, Physical properties of aqueous glycerol solutions. *J. Petrol. Sci. Eng.* **98-99**, 50–60 (2012).
85. Y. Bae, M. Y. Ha, K.-T. Bang, S. Yang, S. Y. Kang, J. Kim, J. Sung, S. Kang, D. Kang, W. B. Lee, T.-L. Choi, J. Park, Conformation dynamics of single polymer strands in solution. *Adv. Mater.* **34**, 2202353 (2022).
86. T. Ando, T. Uchihashi, N. Kodera, High-speed AFM and applications to biomolecular systems. *Annu. Rev. Biophys.* **42**, 393–414 (2013).
87. Y. F. Dufrêne, T. Ando, R. Garcia, D. Alsteens, D. Martinez-Martin, A. Engel, C. Gerber, D. J. Müller, Imaging modes of atomic force microscopy for application in molecular and cell biology. *Nat. Nanotechnol.* **12**, 295–307 (2017).
88. E. Khestanova, F. Guinea, L. Fumagalli, A. K. Geim, I. V. Grigorieva, Universal shape and pressure inside bubbles appearing in van der Waals heterostructures. *Nat. Commun.* **7**, 12587 (2016).
89. S. M. Ghodsi, S. Sharifi-Asl, P. Rehak, P. Král, C. M. Megaridis, R. Shahbazian-Yassar, T. Shokuhfar, Assessment of pressure and density of confined water in graphene liquid cells. *Adv. Mater. Interfaces* **7**, 1901727 (2020).
90. P. Cioni, G. B. Strambini, Effect of heavy water on protein flexibility. *Biophys. J.* **82**, 3246–3253 (2002).
91. Y. M. Efimova, S. Haemers, B. Wierczinski, W. Norde, A. A. van Well, Stability of globular proteins in H2O and D2O. *Biopolymers* **85**, 264–273 (2007).
92. W. Bild, V. Năstasă, I. Haulică, In vivo and in vitro research on the biological effects of deuterium-depleted water: 1. Influence of deuterium-depleted water on cultured cell growth. *Romanian J. Physiol. Physiol. Sci.* **41**, 53–67 (2004).
93. C. Wang, Q. Qiao, T. Shokuhfar, R. F. Klie, High-resolution electron microscopy and spectroscopy of ferritin in biocompatible graphene liquid cells and graphene sandwiches. *Adv. Mater.* **26**, 3410–3414 (2014).
94. M. Textor, N. de Jonge, Strategies for preparing graphene liquid cells for transmission electron microscopy. *Nano Lett.* **18**, 3313–3321 (2018).
95. E. L. Dunnavan, Z. Jiang, A general method for estimating bulk 2D projections of ice particle shape: Theory and applications. *J. Atmos. Sci.* **76**, 305–332 (2019).
96. Z. Jiang, M. Oue, J. Verlinde, E. E. Clothiaux, K. Aydin, G. Botta, Y. Lu, What can we conclude about the real aspect ratios of ice particle aggregates from two-dimensional images? *J. Appl. Meteorol. Climatol.* **56**, 725–734 (2017).
97. D. R. McDougle, A. Kambalyal, D. D. Meling, A. Das, Endocannabinoids anandamide and 2-arachidonoylglycerol Are substrates for human CYP2J2 epoxygenase. *J. Pharmacol. Exp. Ther.* **351**, 616–627 (2014).
98. D. R. McDougle, A. Palaria, E. Magnetta, D. D. Meling, A. Das, Functional studies of N-terminally modified CYP2J2 epoxygenase in model lipid bilayers. *Protein Sci.* **22**, 964–979 (2013).
99. T. H. Bayburt, Y. V. Grinkova, S. G. Sligar, Self-assembly of discoidal phospholipid bilayer nanoparticles with membrane scaffold proteins. *Nano Lett.* **2**, 853–856 (2002).
100. I. G. Denisov, Y. V. Grinkova, A. A. Lazarides, S. G. Sligar, Directed self-assembly of monodisperse phospholipid bilayer nanodiscs with controlled size. *J. Am. Chem. Soc.* **126**, 3477–3487 (2004).
101. S. De Carlo, J. R. Harris, Negative staining and cryo-negative staining of macromolecules and viruses for TEM. *Micron* **42**, 117–131 (2011).
102. R. Dugad, N. Ahuja, "Video denoising by combining Kalman and Wiener estimates" in *Proceedings 1999 International Conference on Image Processing (Cat. 99CH36348)* (IEEE, 1999), vol. 4, pp. 152–156.
103. Q. Tseng, I. Wang, E. Duchemin-Pelletier, A. Azioune, N. Carpi, J. Gao, O. Filhol, M. Piel, M. Théry, M. Balland, A new micropatterning method of soft substrates reveals that different tumorigenic signals can promote or reduce cell contraction levels. *Lab Chip* **11**, 2231–2240 (2011).
104. Q. Tseng, E. Duchemin-Pelletier, A. Deshiere, M. Balland, H. Guillou, O. Filhol, M. Théry, Spatial organization of the extracellular matrix regulates cell–cell junction positioning. *Proc. Natl. Acad. Sci. U.S.A.* **109**, 1506–1511 (2012).
105. W. Helfrich, Elastic properties of lipid bilayers: Theory and possible experiments. *Z. Für Naturforschung C* **28**, 693–703 (1973).
106. V. G. Almendro-Vedia, P. Natale, M. Mell, S. Bonneau, F. Monroy, F. Joubert, I. López-Montero, Nonequilibrium fluctuations of lipid membranes by the rotating motor protein F1F0-ATP synthase. *Proc. Natl. Acad. Sci. U.S.A.* **114**, 11291–11296 (2017).
107. J. Prost, R. Bruinsma, Shape fluctuations of active membranes. *EPL Europhys. Lett.* **33**, 321–326 (1996).
108. S. M. Mousavi, G. Gompper, R. G. Winkler, Active Brownian ring polymers. *J. Chem. Phys.* **150**, 064913 (2019).
109. I. Arganda-Carreras, C. O. S. Sorzano, R. Marabini, J. M. Carazo, C. Ortiz-de-Solorzano, J. Kybic, "Consistent and elastic registration of histological sections using vector-spline regularization" in *Computer Vision Approaches to Medical Image Analysis*, R. R. Beichel, M. Sonka, Eds. (Springer, 2006), pp. 85–95.
110. N. de Jonge, Theory of the spatial resolution of (scanning) transmission electron microscopy in liquid water or ice layers. *Ultramicroscopy* **187**, 113–125 (2018).
111. N. de Jonge, L. Houben, R. E. Dunin-Borkowski, F. M. Ross, Resolution and aberration correction in liquid cell transmission electron microscopy. *Nat. Rev. Mater.* **4**, 61–78 (2019).
112. D. H. de Jong, G. Singh, W. F. D. Bennett, C. Arnarez, T. A. Wassenaar, L. V. Schäfer, X. Periole, D. P. Tieleman, S. J. Marrink, Improved parameters for the Martini coarse-grained protein force field. *J. Chem. Theory Comput.* **9**, 687–697 (2013).
113. L. Monticelli, S. K. Kandasamy, X. Periole, R. G. Larson, D. P. Tieleman, S.-J. Marrink, The MARTINI coarse-grained force field: Extension to proteins. *J. Chem. Theory Comput.* **4**, 819–834 (2008).
114. X. Periole, M. Cavalli, S.-J. Marrink, M. A. Ceruso, Combining an Elastic Network With a Coarse-Grained Molecular Force Field: Structure, Dynamics, and Intermolecular Recognition. *J. Chem. Theory Comput.* **5**, 2531–2543 (2009).
115. S. Jo, T. Kim, V. G. Iyer, W. Im, CHARMM-GUI: A web-based graphical user interface for CHARMM. *J. Comput. Chem.* **29**, 1859–1865 (2008).
116. Y. Qi, H. I. Ingólfsson, X. Cheng, J. Lee, S. J. Marrink, W. Im, CHARMM-GUI Martini maker for coarse-grained simulations with the martini force field. *J. Chem. Theory Comput.* **11**, 4486–4494 (2015).
117. Y. Qi, J. Lee, J. B. Klauda, W. Im, CHARMM-GUI Nanodisc Builder for modeling and simulation of various nanodisc systems. *J. Comput. Chem.* **40**, 893–899 (2019).
118. T. A. Wassenaar, H. I. Ingólfsson, R. A. Böckmann, D. P. Tieleman, S. J. Marrink, Computational lipidomics with insane: A versatile tool for generating custom membranes for molecular simulations. *J. Chem. Theory Comput.* **11**, 2144–2155 (2015).
119. M. Chavent, T. Reddy, J. Goose, A. C. E. Dahl, J. E. Stone, B. Jobard, M. S. P. Sansom, Methodologies for the analysis of instantaneous lipid diffusion in md simulations of large membrane systems. *Faraday Discuss.* **169**, 455–475 (2014).
120. S. Buchoux, FATSLiM: A fast and robust software to analyze MD simulations of membranes. *Bioinformatics* **33**, 133–134 (2017).
121. T. A. Wassenaar, K. Pluhackova, R. A. Böckmann, S. J. Marrink, D. P. Tieleman, Going backward: A flexible geometric approach to reverse transformation from coarse grained to atomistic models. *J. Chem. Theory Comput.* **10**, 676–690 (2014).
122. J. Frank, "Chapter 2 - Electron microscopy of macromolecular assemblies" in *Three-Dimensional Electron Microscopy of Macromolecular Assemblies*, J. Frank, Ed. (Academic Press, 1996), pp. 12–53.
123. D. B. Peckys, P. Mazur, K. L. Gould, N. de Jonge, Fully hydrated yeast cells imaged with electron microscopy. *Biophys. J.* **100**, 2522–2529 (2011).

124. H. Demers, N. Poirier-Demers, A. R. Couture, D. Joly, M. Guilmain, N. de Jonge, D. Drouin, Three-dimensional electron microscopy simulation with the CASINO Monte Carlo software. *Scanning* **33**, 135–146 (2011).
125. K. Zhang, Gctf: Real-time CTF determination and correction. *J. Struct. Biol.* **193**, 1–12 (2016).
126. J. M. Zuo, J. C. H. Spence, "Atomic resolution electron imaging" in *Advanced Transmission Electron Microscopy: Imaging and Diffraction in Nanoscience*, J. M. Zuo, J. C. H. Spence, Eds. (Springer, 2017), pp. 441–499.
127. L. Reimer, "Electron-specimen interactions" in *Transmission Electron Microscopy: Physics of Image Formation and Microanalysis*, L. Reimer, Ed. (Springer, 1993), pp. 136–191.
128. M. Vulović, R. B. G. Ravelli, L. J. van Vliet, A. J. Koster, I. Lazić, U. Lücken, H. Rullgård, O. Öktem, B. Rieger, Image formation modeling in cryo-electron microscopy. *J. Struct. Biol.* **183**, 19–32 (2013).
129. H. Rullgård, L.-G. Öfverstedt, S. Masich, B. Daneholt, O. Öktem, Simulation of transmission electron microscope images of biological specimens. *J. Microsc.* **243**, 234–256 (2011).
130. curtis.suplee@nist.gov, Stopping-Power & Range Tables for Electrons, Protons, and Helium Ions, NIST (2009); www.nist.gov/pml/stopping-power-range-tables-electrons-protons-and-helium-ions.
131. W. J. Dearnaley, B. Schleupner, A. C. Varano, N. A. Alden, F. Gonzalez, M. A. Casasanta, B. E. Scharf, M. J. Dukes, D. F. Kelly, Liquid-cell electron tomography of biological systems. *Nano Lett.* **19**, 6734–6741 (2019).
132. L. M. DiMemmo, A. C. Varano, J. Haulenbeek, Y. Liang, K. Patel, M. J. Dukes, S. Zheng, M. Hubert, S. P. Piccoli, D. F. Kelly, Real-time observation of protein aggregates in pharmaceutical formulations using liquid cell electron microscopy. *Lab Chip* **17**, 315–322 (2017).
133. D. F. Parsons, V. R. Matricardi, R. C. Moretz, J. N. Turner, "Electron microscopy and diffraction of wet unstained and unfixed biological objects" in *Advances in Biological and Medical Physics*, J. H. Lawrence, J. W. Gofman, Eds. (Elsevier, 1974), vol. 15, pp. 161–270.
134. T. Yamazaki, Y. Kimura, P. G. Vekilov, E. Furukawa, M. Shirai, H. Matsumoto, A. E. S. V. Driessche, K. Tsukamoto, Two types of amorphous protein particles facilitate crystal nucleation. *Proc. Natl. Acad. Sci. U.S.A.* **114**, 2154–2159 (2017).
135. V. R. Matricardi, R. C. Moretz, D. F. Parsons, Electron diffraction of wet proteins: Catalase. *Science* **177**, 268–270 (1972).
136. J. K. Yano, M. R. Wester, G. A. Schoch, K. J. Griffin, C. D. Stout, E. F. Johnson, The structure of human microsomal cytochrome P450 3A4 determined by x-ray crystallography to 2.05-Å resolution. *J. Biol. Chem.* **279**, 38091–38094 (2004).

Acknowledgments: We are grateful to E. Tajkhorshid and C. Schroeder of the University of Illinois for insightful feedback on the manuscript. We also thank G. Licari and C. Xu, formerly of the University of Illinois, for helpful discussions and guidance. Experiments were carried out in the Materials Research Laboratory Central Research Facilities and Veterinary Medicine Basic Sciences Building, University of Illinois Urbana–Champaign. **Funding:** This work was supported by the following funding sources: AFOSR grant FA9550-20-1-0257 (to J.S. and Q.C.), AFOSR grant FA9550-23-1-0609 (to J.S., A.D., and Q.C.), AFOSR DURIP grant FA9550-18-1-0393 (to J.S. and Q.C.), and National Institutes of Health grant R01GM115584 (to A.D.). **Author contributions:** Conceptualization: J.W.S., A.D., L.N.C., and Q.C. Formal analysis: J.W.S. and Q.C. Investigation: J.W.S. (liquid phase TEM and simulations); L.N.C. and A.D. (nanodisc preparation and characterization). Methodology: J.W.S., L.N.C., A.D., and Q.C. Validation: J.W.S. and L.N.C. Data curation: L.N.C. and A.D. Formal analysis: J.W.S., L.N.C., and A.D. Software: J.W.S. Supervision: A.D. and Q.C. Visualization: J.W.S., L.N.C., A.D., and Q.C. Writing—original draft: J.W.S., L.N.C., A.D., and Q.C. Writing—review and editing: J.W.S., L.N.C., A.D., and Q.C. Resources: L.N.C., A.D., and Q.C. Funding acquisition: A.D. and Q.C. Project administration: A.D. and Q.C. **Competing interests:** The authors declare that they have no competing interests. **Data and materials availability:** All data needed to evaluate the conclusions in the paper are present in the paper and/or the Supplementary Materials.

Submitted 29 July 2023
Accepted 15 March 2024
Published 17 April 2024
10.1126/sciadv.adk0217